Supplemental Material: Strong Superexchange in a $d^{9-\delta}$ Nickelate Revealed by Resonant Inelastic X-Ray Scattering

(Dated: January 21, 2021)

I. FURTHER DETAILS OF THE SINGLE-CRYSTAL SYNTHESIS

Single-crystal growth of $R_4Ni_3O_{10}$ (R =La, Pr) was performed as described Refs. [1, 2]. The parent Ruddlesden-Popper phases were prepared in a floating zone furnace (HKZ-1, SciDre GmbH) with 20 bar O_2 for R =La and 140 bar for R=Pr. Oxygen was flowed at a rate of 0.1 l/min during growth and the feed and seed rods were counter-rotated at 30 r.p.m. and 27 r.p.m., respectively, to improve zone homogeneity. The traveling speed of the seed was 4 mm/h and the growth time was 30 hours. 438-phase crystals were obtained by reducing the 4310-specimens in 4 mol % H_2/Ar gas at 350°C for five days. The resulting samples have appreciable residual strain and are very brittle, so they were mounted on copper plates for transport.

II. RESONANT BEHAVIOR

In Fig. S1 we show the resonant behavior of the magnon. The magnon peak is visible at several energies from 851.5 to 853.1 eV exhibiting a Raman-like behavior in which it appears at a constant energy loss, rather than a constant final x-ray energy. We find that the magnon is strongest at 852.7 eV (as emphasized by the dashed line at this energy). This is well above the La M_4-edge at 849 eV, further confirming the magnetic origin of the magnon.

III. FITTING OF THE RIXS DATA

The spectra were fitted with a Gaussian function for the elastic peak, a damped harmonic oscillator model for the paramagnon and a quadratic background. The inelastic peak was convoluted with a Gaussian function to account for the energy resolution. This lineshape is described by nine parameters, but only six parameters are free to vary in the fit. For the Gaussian lineshape describing the elastic peak, the center and the width are fixed by measurements of a graphite elastic reference sample, only the amplitude is free to vary. For the inelastic mode, the temperature is fixed, and the center, width and amplitude are free. For the quadratic background, we use a function $f(x) = b$ for $x < 0$

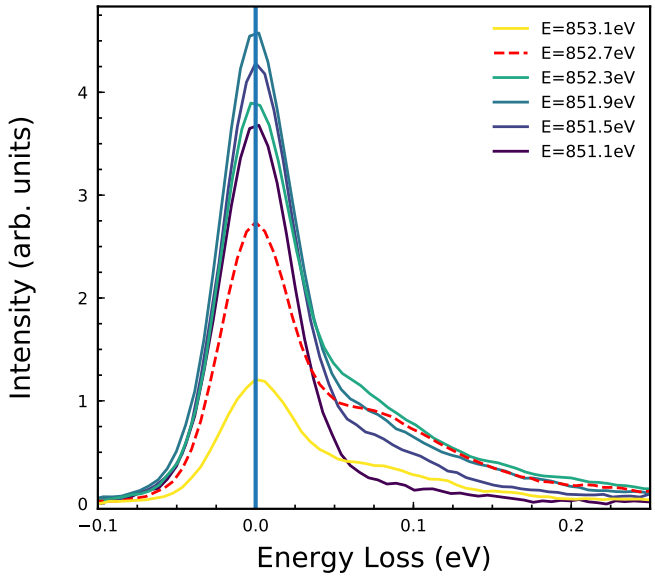

FIG. S1. RIXS spectra of $La_4Ni_3O_8$ at $(-0.44, 0)$ as a function of incident energy around the Ni L_3 edge. The chosen working energy that optimizes the magnon intensity, 852.7 eV, is highlighted using a dashed line and occurs above the maximum in the elastic line resonance, further confirming the magnetic nature of the observed inelastic excitations [3].

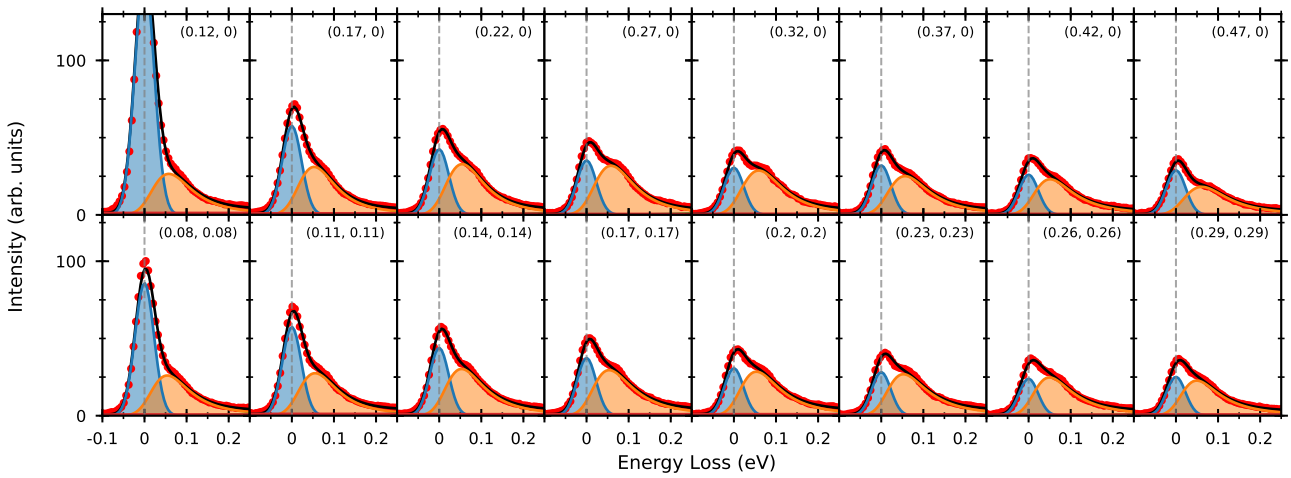

FIG. S2. RIXS spectra of $Pr_4Ni_3O_8$ as a function of $\boldsymbol{Q}$ at the resonant energy of the magnon 852.7 eV. Data are shown as red points and the fit is shown as a black line, which is composed of the magnetic excitation in orange and the elastic line in blue. The in-plane $\boldsymbol{Q}$ of the measured spectrum is denoted in the top right of each panel. Note that the scale of the y-axis is half of that in Fig. 2 of the main text.

and $f(x) = a * x^2 + b$ for $x > 0$, a and b are free parameters. Prior to computing the final fit, we performed an initial fit in which the elastic energy was allowed to vary, which we used to shift the spectra in energy such that the elastic energy is set to exactly zero.

IV. COMPARISON OF $La_4Ni_3O_8$ AND $Pr_4Ni_3O_8$

The difference between $La_4Ni_3O_8$ and $Pr_4Ni_3O_8$ has been studied in prior x-ray absorption and density functional theory (DFT)-based work [2]. This study concluded that both materials are rather similar regarding their high- and medium-energy physics such as spin states, orbital polarization, etc. The primary difference is that stripe order opens a small insulating gap in $La_4Ni_3O_8$, whereas $Pr_4Ni_3O_8$ remains metallic without long-range order. $Pr_4Ni_3O_8$ was later reported to have spin-glass behavior likely coming from short-range stripe correlations [4]. Since the more ordered and insulating nature of $La_4Ni_3O_8$ compared to $Pr_4Ni_3O_8$ is expected to give sharper magnetic RIXS spectra, we focused on the former material for this paper, but we also took data on $Pr_4Ni_3O_8$ as shown in Fig. S2. A similar energy peak is observed which is slightly broadened and less intense compared to $La_4Ni_3O_8$. Fitting the spectra for $Pr_4Ni_3O_8$ in the same way as was done for $La_4Ni_3O_8$ yields a value of the near-neighbor exchange perhaps 10% lower, but overall the two materials are very similar (Fig. S3).

V. THEORY OF MAGNETIC EXCITATIONS IN THE STRIPE-ORDERED STATE

In this Section, we compute the dispersion relation and RIXS intensity for the magnons in a diagonal stripe state. To reproduce the stripe order shown in Fig. 1(b) of the main text, we consider a model with the following interactions illustrated in Fig. S4. J couples nearest-neighbor spins within the same stripe, J_1 couples spins across the stripes in the $[1, 0, 0]$ direction, and J_z couples spins between layers within the trilayer in the $[0, 0, 1]$ direction. A further J_2 coupling across the stripes along the $[1, 1, 0]$ direction was also considered, but its effect could not be distinguished in the measured RIXS spectra, so it was omitted. This is expected as this super-superexchange contribution is weak given the 90 degree Ni-Ni-Ni pathway that is involved. We also ignore any single-ion anisotropy, again because it would be difficult to detect given the width of the elastic line. The in-plane lattice vectors for the structural unit cell are

$$\boldsymbol{a_1} = (a, 0, 0), \quad \boldsymbol{a_2} = (0, a, 0) \tag{1}$$

and for the magnetic unit cell are

$$\boldsymbol{a_1}^{\text{mag}} = (3a, 0, 0), \quad \boldsymbol{a_2}^{\text{mag}} = (-a, a, 0). \tag{2}$$

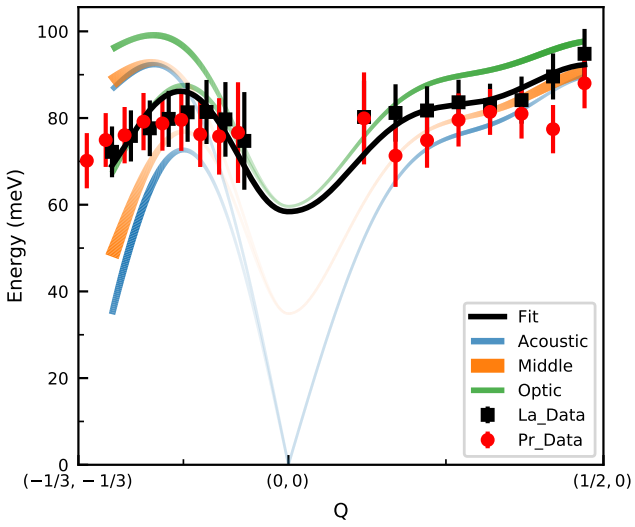

FIG. S3. Magnetic dispersion of $La_4Ni_3O_8$ and $Pr_4Ni_3O_8$. This figure is the same as Fig. 3 of the main text, but with data for $Pr_4Ni_3O_8$ added. Black/red points are the extracted energies of the magnetic excitation for $La_4Ni_3O_8$/$Pr_4Ni_3O_8$. The black line is the fit to the experimental dispersion of $La_4Ni_3O_8$, which is composed of the weighted sum of three dispersive magnons, called the acoustic, middle and optic modes, which are plotted as blue, orange and green lines, respectively.

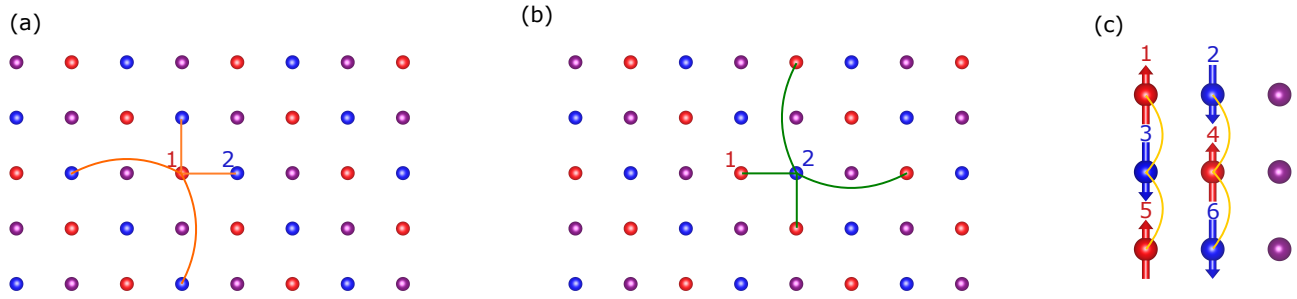

FIG. S4. Coupling of the spins in the stripe-ordered state for: (a) a spin up in the top layer of the trilayer, (b) a spin down in the top layer, and (c) between the different layers. For simplicity, only the Ni sites are shown with red, blue and purple denoting up-spin, down-spin and hole states as in Fig. 1 of the main text.

where, for simplicity, we have assumed a primitive magnetic cell with non-orthogonal lattice vectors. Along the c direction, we have trilayers separated by the body-centered translation $(a/2, a/2, c/2)$. Since there are no observable correlations between trilayers [5], we consider only a single trilayer here. The layers within a trilayer are in registry along c, with each layer separated by the interlayer distance $d \approx c/8$. The scattering vector $\boldsymbol{Q}$ is presented in normalized units with $a = c = 1$.

A. Dispersion relation

We proceed to calculate the magnon dispersion for the diagonal stripe state by generalizing the torque equation formalism of Carlson *et al.* [6] to the trilayer case (equivalent results can be obtained using the less transparent Holstein-Primakoff treatment [6]). According to neutron scattering data, the spins in the ground state are oriented

along c [5]. Therefore, the generalized torque equations for the spins reduce to:

$$\begin{aligned}
\frac{dS^x_{\boldsymbol{r},i}}{dt} &= -\frac{1}{\hbar}\left(S^y_{\boldsymbol{r},i}\sum_{\boldsymbol{r'},j} J^{ij}_{\boldsymbol{rr'}} S^z_{\boldsymbol{r'},j} - S^z_{\boldsymbol{r},i}\sum_{\boldsymbol{r'},j} J^{ij}_{\boldsymbol{rr'}} S^y_{\boldsymbol{r'},j}\right), \\
\frac{dS^y_{\boldsymbol{r},i}}{dt} &= -\frac{1}{\hbar}\left(S^z_{\boldsymbol{r},i}\sum_{\boldsymbol{r'},j} J^{ij}_{\boldsymbol{rr'}} S^x_{\boldsymbol{r'},j} - S^x_{\boldsymbol{r},i}\sum_{\boldsymbol{r'},j} J^{ij}_{\boldsymbol{rr'}} S^z_{\boldsymbol{r'},j}\right), \\
\frac{dS^z_{\boldsymbol{r},i}}{dt} &\approx 0,
\end{aligned} \tag{3}$$

where $\boldsymbol{r}, \boldsymbol{r'}$ label the positions of the spins in different magnetic unit cells and the indices i, j label the spins within each magnetic unit cell ($i, j = 1, ..., 6$) as shown in Fig. S2. We seek sinusoidal solutions of the form

$$S^x_{\boldsymbol{r},i} = S^x_i \exp[i(\boldsymbol{Q}\cdot\boldsymbol{r} - \omega t)] \ , \quad S^y_{\boldsymbol{r},i} = S^y_i \exp[i(\boldsymbol{Q}\cdot\boldsymbol{r} - \omega t)], \tag{4}$$

and we set $S^z_{\boldsymbol{r},i} = \pm S$ with the sign given by the orientation of the spin in the ground state. To start, we identify the couplings $J^{ij}_{\boldsymbol{rr'}}$ that connect the spins at different lattice positions, with the origin taken to be the location of spin 1. We distinguish two groups of spins, (S_1, S_3, S_5) and (S_2, S_4, S_6), with each group having equivalent in-plane locations due to the c-axis translational symmetry. Their couplings are

- S_1 ($\boldsymbol{r} = \boldsymbol{0}$) couples to S_2 twice with J ($\boldsymbol{r'} = \boldsymbol{a_1}$, $\boldsymbol{r'} = \boldsymbol{a_2}$) and twice with J_1 ($\boldsymbol{r'} = -2\boldsymbol{a_1}$, $\boldsymbol{r'} = -2\boldsymbol{a_2}$). The same applies for S_3 (S_5) coupled to S_4 (S_6).
- S_2 ($\boldsymbol{r} = \boldsymbol{a_1}$) couples to S_1 twice with J ($\boldsymbol{r'} = \boldsymbol{0}$, $\boldsymbol{r'} = \boldsymbol{a_1} - \boldsymbol{a_2}$) and twice with J_1 ($\boldsymbol{r'} = 3\boldsymbol{a_1}$, $\boldsymbol{r'} = \boldsymbol{a_1} + 2\boldsymbol{a_2}$). The same applies for S_4 (S_6) coupled to S_3 (S_1).

For the couplings along [0,0,1], we have:

- S_1 (S_2) couples to S_3 (S_4) with J_z.
- S_5 (S_6) couples to S_3 (S_4) with J_z.
- S_3 (S_4) couples with J_z to S_1 (S_2) and to S_5 (S_6).

With this information, we can write the torque equations for each of the six spins in the magnetic unit cell, for example:

$$\begin{aligned}
\frac{dS^x_{\boldsymbol{0},1}}{dt} = -\frac{1}{\hbar}\Bigg\{ & S^y_{\boldsymbol{0},1}(-S)\Big(2J + 2J_1 + J_z\Big) \\
& - S\left[J\Big(S^y_{\boldsymbol{a_1},2} + S^y_{\boldsymbol{a_2},2}\Big) + J_1\Big(S^y_{-2\boldsymbol{a_1},2} + S^y_{-2\boldsymbol{a_2},2}\Big) + J_z\Big(S^y_{(0,0,-\frac{c}{8}),3}\Big)\right]\Bigg\}.
\end{aligned} \tag{5}$$

Substituting Eq. 4, we can rewrite this expression as

$$\begin{aligned}
\frac{i\hbar\omega}{S}S^x_1 = & -S^y_1\Big(2J + 2J_1 + J_z\Big) - S^y_3 J_z e^{-i\frac{Q_z}{8}} \\
& - S^y_2\left[J\Big(e^{iQ_x} + e^{iQ_y}\Big) + J_1\Big(e^{-2iQ_x} + e^{-2iQ_y}\Big)\right],
\end{aligned} \tag{6}$$

and simplifying

$$\frac{i\hbar\omega}{S}S^x_1 = -AS^y_1 - CS^y_2 - DS^y_3, \tag{7}$$

where we have defined

$$\begin{aligned}
A &= 2J + 2J_1 + J_z, \\
B &= A + J_z, \\
C &= J\left(e^{iQ_x} + e^{iQ_y}\right) + J_1\left(e^{-2iQ_x} + e^{-2iQ_y}\right), \\
D &= J_z e^{-i\frac{Q_z}{8}}.
\end{aligned} \tag{8}$$

The final torque equations for the six spins are

$$\begin{aligned}
\frac{i\hbar\omega}{S}S_1^x &= -AS_1^y - CS_2^y - DS_3^y, & \frac{i\hbar\omega}{S}S_1^y &= +AS_1^x + CS_2^x + DS_3^x \\
\frac{i\hbar\omega}{S}S_2^x &= +AS_2^y + C^*S_1^y + DS_4^y, & \frac{i\hbar\omega}{S}S_2^y &= -AS_2^x - C^*S_1^x - DS_4^x \\
\frac{i\hbar\omega}{S}S_3^x &= +BS_3^y + CS_4^y + DS_5^y + D^*S_1^y, & \frac{i\hbar\omega}{S}S_3^y &= -BS_3^x - CS_4^x - DS_5^x - D^*S_1^x \\
\frac{i\hbar\omega}{S}S_4^x &= -BS_4^y - C^*S_3^y - DS_6^y - D^*S_2^y, & \frac{i\hbar\omega}{S}S_4^y &= +BS_4^x + C^*S_3^x + DS_6^x + D^*S_2^x \\
\frac{i\hbar\omega}{S}S_5^x &= -AS_5^y - CS_6^y - D^*S_3^y, & \frac{i\hbar\omega}{S}S_5^y &= +AS_5^x + CS_6^x + D^*S_3^x \\
\frac{i\hbar\omega}{S}S_6^x &= +AS_6^y + C^*S_5^y + D^*S_4^y, & \frac{i\hbar\omega}{S}S_6^y &= -AS_6^x - C^*S_5^x - D^*S_4^x.
\end{aligned} \tag{9}$$

This results in a 12×12 secular matrix (6 spins, 2 components, x, y, per spin)

$$M = \begin{pmatrix}
0 & -A & 0 & -C & 0 & -D & 0 & 0 & 0 & 0 & 0 & 0 \\
A & 0 & C & 0 & D & 0 & 0 & 0 & 0 & 0 & 0 & 0 \\
0 & C^* & 0 & A & 0 & 0 & 0 & D & 0 & 0 & 0 & 0 \\
-C^* & 0 & -A & 0 & 0 & 0 & -D & 0 & 0 & 0 & 0 & 0 \\
0 & D^* & 0 & 0 & 0 & B & 0 & C & 0 & D & 0 & 0 \\
-D^* & 0 & 0 & 0 & -B & 0 & -C & 0 & -D & 0 & 0 & 0 \\
0 & 0 & 0 & -D^* & 0 & -C^* & 0 & -B & 0 & 0 & 0 & -D \\
0 & 0 & D^* & 0 & C^* & 0 & B & 0 & 0 & 0 & D & 0 \\
0 & 0 & 0 & 0 & 0 & -D^* & 0 & 0 & 0 & -A & 0 & -C \\
0 & 0 & 0 & 0 & D^* & 0 & 0 & 0 & A & 0 & C & 0 \\
0 & 0 & 0 & 0 & 0 & 0 & 0 & D^* & 0 & C^* & 0 & A \\
0 & 0 & 0 & 0 & 0 & 0 & -D^* & 0 & -C^* & 0 & -A & 0
\end{pmatrix}. \tag{10}$$

Diagonalizing this matrix yields the squared eigenvalues

$$\lambda_1^2(\boldsymbol{Q}) = -A^2 + C^*C \tag{11}$$

and

$$\lambda_{2,3}^2(\boldsymbol{Q}) = -\frac{A^2}{2} - \frac{B^2}{2} + C^*C + 2J_z^2 \pm \frac{1}{2}J_z\sqrt{(A+B)^2 + 32C^*C - 8J_z^2}, \tag{12}$$

each of which are two-fold degenerate because of the tetragonal symmetry of the ground state. As $i\omega = \lambda$, these eigenvalues correspond to the magnon branches

$$\omega_{\text{middle}}(\boldsymbol{Q}) = \sqrt{A^2 - C^*C} \tag{13}$$

and

$$\omega_{\text{acoustic,optic}}(\boldsymbol{Q}) = \sqrt{\frac{A^2}{2} + \frac{B^2}{2} - C^*C - 2J_z^2 \mp \frac{1}{2}J_z\sqrt{(A+B)^2 + 32C^*C - 8J_z^2}}. \tag{14}$$

To justify these labels, and give some sense of these energies, we consider the Γ point. Substituting $\boldsymbol{Q} = 0$ in Eq. 8 gives $C = 2J + 2J_1$ and $D = J_z$, which shows that our labels were chosen in order of increasing energy:

$$\begin{aligned}
&\omega_{\text{acoustic}}(\mathbf{0}) = 0, \\
&\omega_{\text{middle}}(\mathbf{0}) = SJ_z\sqrt{1 + 2C/J_z} \sim S\sqrt{2J_zC}, \\
&\omega_{\text{optic}}(\mathbf{0}) = SJ_z\sqrt{1 + 6C/J_z} \sim S\sqrt{6J_zC},
\end{aligned} \tag{15}$$

where the approximation applies for $J_z \ll J$. The magnon dispersion for the parameters determined by the fit to the RIXS data, J=69 meV, J_1=17 meV (with J_z=13.6 meV), can be seen in Fig. S5.

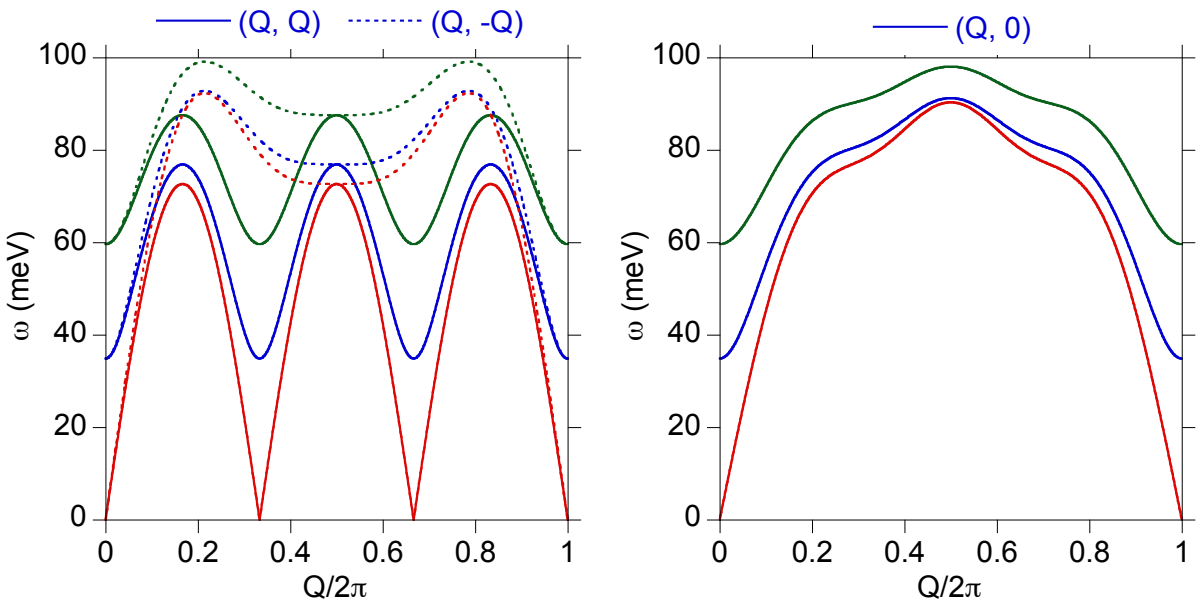

FIG. S5. Magnon dispersion with J=69 meV, J_1=17 meV and J_z=13.6 meV, as in the main text, along the (Q,Q) and (Q,0) directions (with Q_z=0). The dashed curves in the left plot are for the twin domain (Q,-Q).

B. Calculation of the RIXS intensities

As explained in the main text and Ref. [7], the RIXS intensity for each mode, labeled n, can be written as

$$I_n(\boldsymbol{Q}) = \left| \sum_i \boldsymbol{k}_{in} \cdot \boldsymbol{M}_{n,\boldsymbol{Q}}(\boldsymbol{r}_i) \right|^2 , \tag{16}$$

with i summed over the six spins in the magnetic unit cell and

$$\boldsymbol{M}_{n,\boldsymbol{Q}}(\boldsymbol{r}_i) = \left(c^x_{n,\boldsymbol{Q},i} S^x_i, c^y_{n,\boldsymbol{Q},i} S^y_i, 0 \right). \tag{17}$$

As the analytic expressions for the eigenvectors are complicated, we chose to determine them by diagonalizing the secular matrix Eq. 10 numerically for each $\boldsymbol{Q}$ using SciPy [8]. As noted above, each distinct magnon branch within our model has two degenerate eigenvalues, with the two members of each pair related by a 90 degree in-plane rotation because of the tetragonal symmetry. That is

$$\left(c^x_1, c^y_1, c^x_2, c^y_2, ...\right) \tag{18}$$

is degenerate with

$$\left(-c^y_1, c^x_1, -c^y_2, c^x_2, ...\right) \tag{19}$$

with $n, \boldsymbol{Q}$ being implicit. It is important to enforce this symmetry when calculating the RIXS intensity.

For the fit shown in the text, we took into account the scattering geometry of the RIXS measurements, with

$$\boldsymbol{k}_{in} = \cos\theta \boldsymbol{I} - \sin\theta \boldsymbol{Q}, \tag{20}$$

and

$$|\boldsymbol{Q}| = \frac{4\pi \sin\theta}{\lambda_E} \tag{21}$$

with θ the Bragg angle and λ_E the photon wavelength. Here,

$$\boldsymbol{I} = \frac{\boldsymbol{Q} \times \boldsymbol{c} \times \boldsymbol{Q}}{|\boldsymbol{c} \times \boldsymbol{Q}|}. \tag{22}$$

In particular, as the in-plane component of $\boldsymbol{Q}$ is swept, the Q_z component changes accordingly.

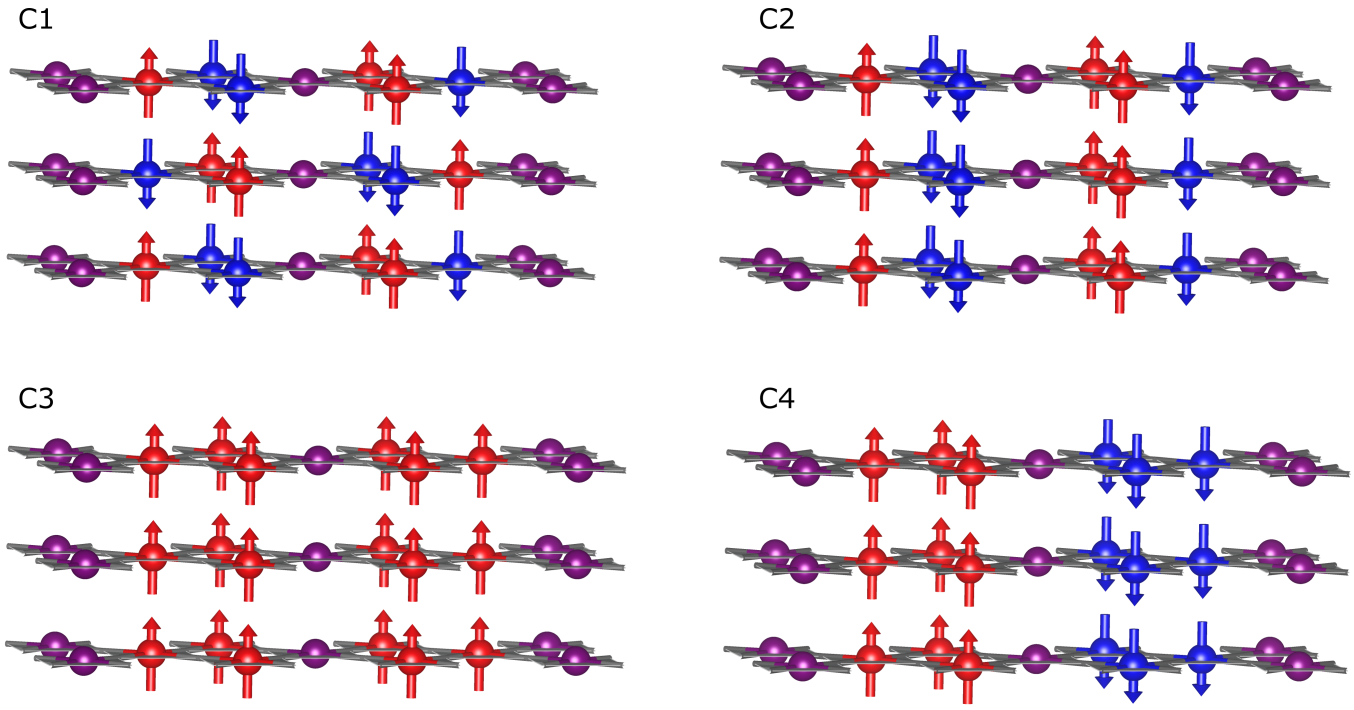

FIG. S6. Magnetic supercells used for determining the magnetic exchange. Ni sites are shown as spheres with red, blue and purple denoting up-spin, down-spin and hole states, respectively, as in Fig. 1 of the main text and Fig. S4. Gray lines trace the Ni-O bond network. Each magnetic cell is a $3\sqrt{2}a \times \sqrt{2}a \times c$ tiling of the structural cell containing 36 Ni atoms (180 atoms in total), noting that there are two trilayer units a given unit cell. Atoms that are at the edge of the unit cell are shown as full spheres rather than being cut-off.

VI. FIRST-PRINCIPLES DETERMINATION OF EXCHANGE COUPLING CONSTANTS IN $La_4Ni_3O_8$

We performed DFT calculations for $La_4Ni_3O_8$ with the all-electron full potential code WIEN2k [9, 10] using the generalized gradient approximation (GGA) exchange-correlation functional [11]. In these calculations, as we did previously [2, 12], we considered the influence of thee Coulomb interaction, U. The U modification of DFT is usually included to compensate for the under-localization of transition-metal $3d$-electrons in DFT. Including U, conversely, tends to over-localize electrons as it "double counts" the true Coulomb and exchange interactions as explained in, for example, Refs. [13–15]. Because of this, it is not immediately obvious whether including U leads to a more accurate value of J. In calculations, we found that the inclusion of U simply increases the size of the gap, and also leads to a modest increase in J, as outlined in Table I. Calculations with and without U find the same insulating, charge and spin stripe-ordered ground state, which was predicted before this state was experimentally observed [5]. In our prior work, we examined the role of U at length and found that the low-spin stripe state $La_4Ni_3O_8$ was appropriately described by GGA calculations even without the inclusion of U [2, 12]. We refer the reader to these papers for the reasoning behind this. Since it allows us to compute J with fewer adjustable parameters, we report values from GGA calculations in the main text, and find that this is in good accord with experiment. As is evident based on how J changes with U, the very close match between theory and experiment of 2 meV at the GGA level is likely coincidental. We note that similar values for the superexchange can be obtained from rough estimates using a sum of the Mott and charge transfer contributions, $J = 2t^2/U_d + 2t^2/[\Delta + U_p/2]$, with $t = t_{pd}^2/\Delta$. Using $U_d = 8.5$ eV and $U_p = 7.3$ eV values from a similar analysis on the cuprates [16], with a Δ and t_{pd} obtained from our Wannier fit for $La_4Ni_3O_8$ [17], a comparable J of 99 meV is obtained. But this, obviously, depends on the choice of U_d and U_p. Spin-orbit coupling is not expected to have an appreciable effect on the exchange constants for $3d$ transition metal ions, especially for e_g states where the orbital moment is largely quenched. This has been explicitly verified in our prior calculations [5].

The exchange couplings (J, J_1 and J_z) were obtained from total energy calculations for different Ni spin configurations (labeled C1-C4 in Fig. S6) mapped to a Heisenberg model. Configuration C1 is the experimental and theoretical ground state as shown in Fig. 1 of the main text. The magnitudes of the magnetic moments of the Ni^{2+} atoms were between 0.6-0.7 μ_B and we confirmed that these values were similar within 0.1 μ_B in the different configurations, an accuracy typical of this type of calculation, justifying the Heisenberg mapping. Different configurations C1-C4 have

differing magnetic bonds:

- C1 – AFM J, AFM J_1, AFM J_z
- C2 – AFM J, AFM J_1, FM J_z
- C3 – FM J, FM J_1, FM J_z
- C4 – FM J, AFM J_1, FM J_z

The energies per trilayer are (with each bond counted once)

$$\begin{aligned} E_{\mathrm{C1}} &= E_0 - 4\times 3JS^2 - 3\times 4J_1S^2 - 2\times 4J_zS^2 \\ &= E_0 - 3J - 3J_1 - 2J_z \\ E_{\mathrm{C2}} &= E_0 - 3J - 3J_1 + 2J_z \\ E_{\mathrm{C3}} &= E_0 + 3J + 3J_1 + 2J_z \\ E_{\mathrm{C4}} &= E_0 + 3J - 3J_1 + 2J_z \end{aligned} \tag{23}$$

where E_0 is the non-magnetic energy. Solving this set of linear equations gives

$$\begin{aligned} J &= (E_{\mathrm{C4}} - E_{\mathrm{C2}})/6 \\ J_1 &= (E_{\mathrm{C3}} - E_{\mathrm{C4}})/6 \\ J_z &= (E_{\mathrm{C2}} - E_{\mathrm{C1}})/4. \end{aligned} \tag{24}$$

whose values are listed in the main text.

VII. X-RAY ABSORPTION

Our X-ray absorption spectrum (XAS) measurements aim to compare the intensity of the O K-edge pre-peak feature as a guide to the $3d$-$2p$ orbital hybridization in nickelates and cuprates. We analyze our data on $La_4Ni_3O_8$ against literature data for $La_{2-x}Sr_xCuO_4$ from Ref. [18] and $Nd_{1-x}Sr_xNiO_2$ from Ref. [19]. As far as we are aware, $Nd_{1-x}Sr_xNiO_2$ data are only available for in-plane polarization, so we only show this component of the polarization. The intensity of the spectra are scaled to have equivalent intensities for energies above 538 eV past the main O K-edge step. Since different measurements can have different absolute energy calibrations, we used measurements of different reference samples to put the spectra on the same energy-scale. We use Ref. [2] as our reference energy calibration for which $La_4Ni_3O_8$ was measured alongside $La_{2-x}Sr_xCuO_4$ and $SrTiO_3$. We then used the $SrTiO_3$ reference measurements in [19] to put $Nd_{1-x}Sr_xNiO_2$ on the same energy scale. While in $La_4Ni_3O_8$ and $La_{2-x}Sr_xCuO_4$ the pre-peak is very clear, the pre-peak in $Nd_{1-x}Sr_xNiO_2$ is broader making isolating the pre-peak less immediately obvious. We took the same 'background' intensity as was used in [19], which comes from a measurement of undoped $NdNiO_2$ and use a lorentzian lineshape to fit. The dominant error in our analysis likely comes from inhomogeneity in the doping of the $Nd_{1-x}Sr_xNiO_2$ results we compare to and some uncertainty in how to isolate all the intensity in the pre-peak. These will likely improve in the future by higher quality sample preparation. Further analysis of the ligand-hole anisotropy will also be important, but also requires polarization-dependent measurements of $Nd_{1-x}Sr_xNiO_2$ that are not currently available in the literature.

[1] Junjie Zhang, Yu-Sheng Chen, D. Phelan, Hong Zheng, M. R. Norman, and J. F. Mitchell, "Stacked charge stripes in the quasi-2D trilayer nickelate $La_4Ni_3O_8$," Proceedings of the National Academy of Sciences **113**, 8945–8950 (2016).

TABLE I. Exchange constants in the GGA and GGA+U approximations ($U = 4.75$ eV).

Exchange constant	GGA+U (meV)	GGA (meV)	Exchange ratio	GGA+U	GGA
J	97.60	71.40	J/J_z	5.04	5.25
J_1	14.28	10.65	J/J_1	6.83	6.7
J_z	19.38	13.6	J_z/J_1	1.36	1.28

[2] Junjie Zhang, AS Botana, JW Freeland, D Phelan, Hong Zheng, V Pardo, MR Norman, and JF Mitchell, "Large orbital polarization in a metallic square-planar nickelate," Nature Physics **13**, 864–869 (2017).

[3] G. Fabbris, D. Meyers, L. Xu, V. M. Katukuri, L. Hozoi, X. Liu, Z.-Y. Chen, J. Okamoto, T. Schmitt, A. Uldry, B. Delley, G. D. Gu, D. Prabhakaran, A. T. Boothroyd, J. van den Brink, D. J. Huang, and M. P. M. Dean, "Doping dependence of collective spin and orbital excitations in the spin-1 quantum antiferromagnet $La_{2-x}Sr_xNiO_4$ observed by x rays," Phys. Rev. Lett. **118**, 156402 (2017).

[4] Shangxiong Huangfu, Zurab Guguchia, Denis Cheptiakov, Xiaofu Zhang, Hubertus Luetkens, Dariusz Jakub Gawryluk, Tian Shang, Fabian O. von Rohr, and Andreas Schilling, "Short-range magnetic interactions and spin-glass behavior in the quasi-two-dimensional nickelate $Pr_4Ni_3O_8$," Phys. Rev. B **102**, 054423 (2020).

[5] Junjie Zhang, D. M. Pajerowski, A. S. Botana, Hong Zheng, L. Harriger, J. Rodriguez-Rivera, J. P. C. Ruff, N. J. Schreiber, B. Wang, Yu-Sheng Chen, W. C. Chen, M. R. Norman, S. Rosenkranz, J. F. Mitchell, and D. Phelan, "Spin stripe order in a square planar trilayer nickelate," Phys. Rev. Lett. **122**, 247201 (2019).

[6] E. W. Carlson, D. X. Yao, and D. K. Campbell, "Spin waves in striped phases," Phys. Rev. B **70**, 064505 (2004).

[7] M. W. Haverkort, "Theory of resonant inelastic x-ray scattering by collective magnetic excitations," Phys. Rev. Lett. **105**, 167404 (2010).

[8] Pauli Virtanen, Ralf Gommers, Travis E. Oliphant, Matt Haberland, Tyler Reddy, David Cournapeau, Evgeni Burovski, Pearu Peterson, Warren Weckesser, Jonathan Bright, Stéfan J. van der Walt, Matthew Brett, Joshua Wilson, K. Jarrod Millman, Nikolay Mayorov, Andrew R. J. Nelson, Eric Jones, Robert Kern, Eric Larson, CJ Carey, İlhan Polat, Yu Feng, Eric W. Moore, Jake Van der Plas, Denis Laxalde, Josef Perktold, Robert Cimrman, Ian Henriksen, E. A. Quintero, Charles R Harris, Anne M. Archibald, Antônio H. Ribeiro, Fabian Pedregosa, Paul van Mulbregt, and SciPy 1.0 Contributors, "SciPy 1.0: Fundamental Algorithms for Scientific Computing in Python," Nature Methods **17**, 261–272 (2020).

[9] P. Blaha, K. Schwarz, G. K. H. Madsen, D. Kvasnicka, J. Luitz, R. Laskowski, F. Tran, and L. D. Marks, *WIEN2k, An Augmented Plane Wave + Local Orbitals Program for Calculating Crystal Properties* (Karlheinz Schwarz, Techn. Universität Wien, Austria, 2018).

[10] Peter Blaha, Karlheinz Schwarz, Fabien Tran, Robert Laskowski, Georg K. H. Madsen, and Laurence D. Marks, "WIEN2k: an APW+lo program for calculating the properties of solids," The Journal of Chemical Physics **152**, 074101 (2020), https://doi.org/10.1063/1.5143061.

[11] John P. Perdew, Kieron Burke, and Matthias Ernzerhof, "Generalized gradient approximation made simple," Phys. Rev. Lett. **77**, 3865–3868 (1996).

[12] Antia S. Botana, Victor Pardo, Warren E. Pickett, and Michael R. Norman, "Charge ordering in Ni^{1+}/Ni^{2+} nickelates: $La_4Ni_3O_8$ and $La_3Ni_2O_6$," Phys. Rev. B **94**, 081105 (2016).

[13] Erik R. Ylvisaker, Warren E. Pickett, and Klaus Koepernik, "Anisotropy and magnetism in the LSDA + U method," Phys. Rev. B **79**, 035103 (2009).

[14] Hanghui Chen and Andrew J. Millis, "Spin-density functional theories and their $+U$ and $+J$ extensions: A comparative study of transition metals and transition metal oxides," Phys. Rev. B **93**, 045133 (2016).

[15] Siheon Ryee and Myung Joon Han, "The effect of double counting, spin density, and hund interaction in the different DFT+U functionals," Scientific reports **8**, 1–11 (2018).

[16] A. K. McMahan, James F. Annett, and Richard M. Martin, "Cuprate parameters from numerical wannier functions," Phys. Rev. B **42**, 6268–6282 (1990).

[17] Emilian M. Nica, Jyoti Krishna, Rong Yu, Qimiao Si, Antia S. Botana, and Onur Erten, "Theoretical investigation of superconductivity in trilayer square-planar nickelates," Phys. Rev. B **102**, 020504 (2020).

[18] C. T. Chen, L. H. Tjeng, J. Kwo, H. L. Kao, P. Rudolf, F. Sette, and R. M. Fleming, "Out-of-plane orbital characters of intrinsic and doped holes in $La_{2-x}Sr_xCuO_4$," Phys. Rev. Lett. **68**, 2543–2546 (1992).

[19] Berit H. Goodge, Danfeng Li, Kyuho Lee, Motoki Osada, Bai Yang Wang, George A. Sawatzky, Harold Y. Hwang, and Lena F. Kourkoutis, "Doping evolution of the mott–hubbard landscape in infinite-layer nickelates," Proceedings of the National Academy of Sciences **118** (2021), 10.1073/pnas.2007683118, https://www.pnas.org/content/118/2/e2007683118.full.pdf.